International Journal of Greenhouse Gas Control 108 (2021) 103315

Contents lists available at ScienceDirect

International Journal of Greenhouse Gas Control

journal homepage: www.elsevier.com/locate/ijggc

Probabilistic analysis of Vette fault stability in potential CO_2 storage site Smeaheia, offshore Norway

Md Jamilur Rahman [a,*], Jung Chan Choi [b], Manzar Fawad [a], Nazmul Haque Mondol [a,b]

[a] Department of Geosciences, University of Oslo (UiO), Sem Sælands vei 1, 0371, Oslo, Norway
[b] Norwegian Geotechnical Institute (NGI), Sognsveien 72, 0806, Oslo, Norway

ARTICLE INFO

Keywords:
Fault stability
Probability of failure
FORM method
Monte-Carlo simulation
System reliability
Uncertainty
Sensitivity

ABSTRACT

Reliable assessment of fault stability is key for safe CO_2 storage in a saline aquifer in fault-bounded structures. The Alpha structure located in the Vette fault's footwall in the Smeaheia area, offshore Norway, is one of the potential CO_2 storage sites with a fault-bounded three-way closure. Assessing fault stability in the Smeaheia area is challenging because of the uncertainties associated with the subsurface fault properties (i.e., fault rock lithologies, strength and geometry of faults, etc.). Besides, CO_2 injection-related pore pressure changes is another critical factor for mechanical deformation and potential failure. We employed a stochastic analytical approach to assess the probability of Vette fault failure using the Monte Carlo Simulation (MCS) and First Order Reliability Method (FORM). The possible fault smear scenarios of the Vette fault zone are evaluated by interpreting the seismic section and the detailed geological understanding. Each scenario's likelihood and the corresponding probability of failure are then integrated stochastically using an event tree method. Overall, Vette fault's system reliability shows a good to average performance range, which has a system probability of failure between 10^{-3} to 10^{-4}. This finding suggests that the Vette fault will likely act as a potential barrier during CO_2 injection into the Alpha structure. Moreover, the sensitivity study reveals that the stresses (both horizontal and vertical) and fault rock strength (i.e., cohesion and friction angle) are the most crucial parameters to characterize uncertainty reduction.

1. Introduction

Capture and geological storage of CO_2 into a saline aquifer is a proven technology to mitigate anthropogenic greenhouse gas emissions into the atmosphere (IPCC, 2005). The CCS technique has already been demonstrated as a safe and reliable solution by several pilot projects worldwide (i.e., Snøhvit, Norway, Chiaramonte et al., 2011; In Salah, Algeria, Mathieson et al., 2010; Sleipner, Norway, Baklid et al., 1996; Ketzin, Germany, Martens et al., 2012; Otway, Australia, Hortle et al., 2013; Quest, Canada, Rock et al., 2017). In partnership with the oil and gas industries, the Norwegian government has evaluated some sites in the Norwegian Continental Shelf (NCS) and developed a strategy for large-scale (Gt storage potential) geological CO_2 sequestration. Smeaheia area is one of the potential sites containing the fault-bounded structural closures Alpha (32/4-1) and Beta (32/2-1), investigated by Equinor and Gassonova (NPD CO_2 Atlas, 2014) (Fig. 1). The area is located east of the Troll East Field, bounded by two major faults; Vette fault (VF) in the west and Øygarden fault complex (ØFC) in the east. The Alpha structure is located in the VF's footwall, whereas the Beta structure is located in the hanging wall of the ØFC (Mulrooney et al., 2018). Fault stability of the Alpha structure could be the critical factor that needs to be evaluated before any CO_2 injection-related activity in the area. However, because of the uncertainties in the subsurface associated with fault properties (i.e., fault rock lithologies, strength, and geometry of fault), it poses a significant challenge to assess the Vette fault's stability.

In addition to the inherent subsurface uncertainties, operational uncertainties associated with pore pressure change during CO_2 injection into a saline aquifer can be another critical factor, which changes the effective stress (i.e., principal stress minus pore pressure) and influences mechanical rock deformation and failure (Verdon et al., 2013). The elastic behavior of pore fluid under the drainage condition is one of the critical factors affecting the mechanical behavior and the stress path of oil field reservoirs, known as a poroelastic effect (Addis, 1997; Grasso, 1992; Hillis, 2001; Segall, 1989). In the case of a supercritical CO_2 (sCO_2) injection, additional processes such as hydraulic aperture

* Corresponding author.
E-mail address: m.j.rahman@geo.uio.no (M.J. Rahman).

https://doi.org/10.1016/j.ijggc.2021.103315
Received 9 November 2020; Received in revised form 15 March 2021; Accepted 20 March 2021
Available online 31 March 2021

evolution, hydrological property changes, effective stress induction, and mechanical strength degradation can influence the effective stresses in fault planes, which can be leading to reactivation and failure of faults (Park et al., 2020; Rutqvist et al., 2007). Although many North Sea faults are proven to have effective sealing properties by supporting considerable hydrocarbon columns (Yielding, 2002), there is still high uncertainty associated with dynamic pressure buildup related to CO_2 injection and wettability of a CO_2-brine-fault rock system (Karolytė et al., 2020; Miocic et al., 2019), also resulting in the potential failure of faults and caprock (Skurtveit et al., 2018). Therefore, a careful investigation of the relation between the fault rock properties, in-situ stresses, and pore pressure perturbation is required to prevent any risk related to CO_2 injection (Chiaramonte et al., 2015).

The potential fault failure can be assessed using either analytical or numerical methods where both approaches have their advantages and disadvantages. This study only considered the analytical techniques, which estimate the fault stability from the theoretical calculations of fault plane stress states and its distance to its nearest shear strength, which generally relies on the Coulomb failure criterion for shear strength calculation (Bohloli et al., 2015; Park et al., 2020). The critical fault slip pressure and fault stability threshold can be determined from the fault's internal properties such as fault orientation, fault material strength, etc. (Vidal-Gilbert et al., 2010; Wiprut and Zoback, 2000) as well as its in-situ stresses. Though analytical methods rely on many assumptions and simplifications for a complicated hydro-mechanical process, these have been proven as useful tools in the preliminary assessment.

The fault zone's structural complexity and the poor seismic resolution along fault make it complicated to predict the fault rock strength (i.e., clay/shale smear, sandstone fragments, mixed lithology, etc.). The fault zone architecture, the distribution of fault rock within the fault zones, and its capacity to seal are still not well-understood, though many research and publications are available (e.g., Faulkner et al., 2010; Færseth, 2006; Færseth et al., 2007, 1984; Gibson, 1994; Jev et al., 1993; Kim et al., 2003; Yielding et al., 1997; Zieglar, 1992). The wettability properties of fault rock and fault rock composition are highly uncertain and significantly different compared with the hydrocarbon system (Miocic et al., 2019). Moreover, most fault zones are beyond seismic resolution and containing several major slip surfaces (Childs et al., 1997; Doughty, 2003; Færseth et al., 2007; Foxford et al., 1998; Gibson, 1994; Walsh et al., 1998). These problems result in inaccuracies in the prediction and quantification of fault rock failure. The shale smearing within the fault zone depends on the relation between fault throw and the amount of clay and shale in the host rock (Bouvier et al., 1989; Fisher and Knipe, 2001; Lindsay et al., 1993; Skerlec, 1996; Yielding et al., 1997). The shalier the host rock is the higher proportion of clay lining that forms in the fault zone, causing a higher capillary entry pressure. The higher the fault throw, the less possibility of having continuous

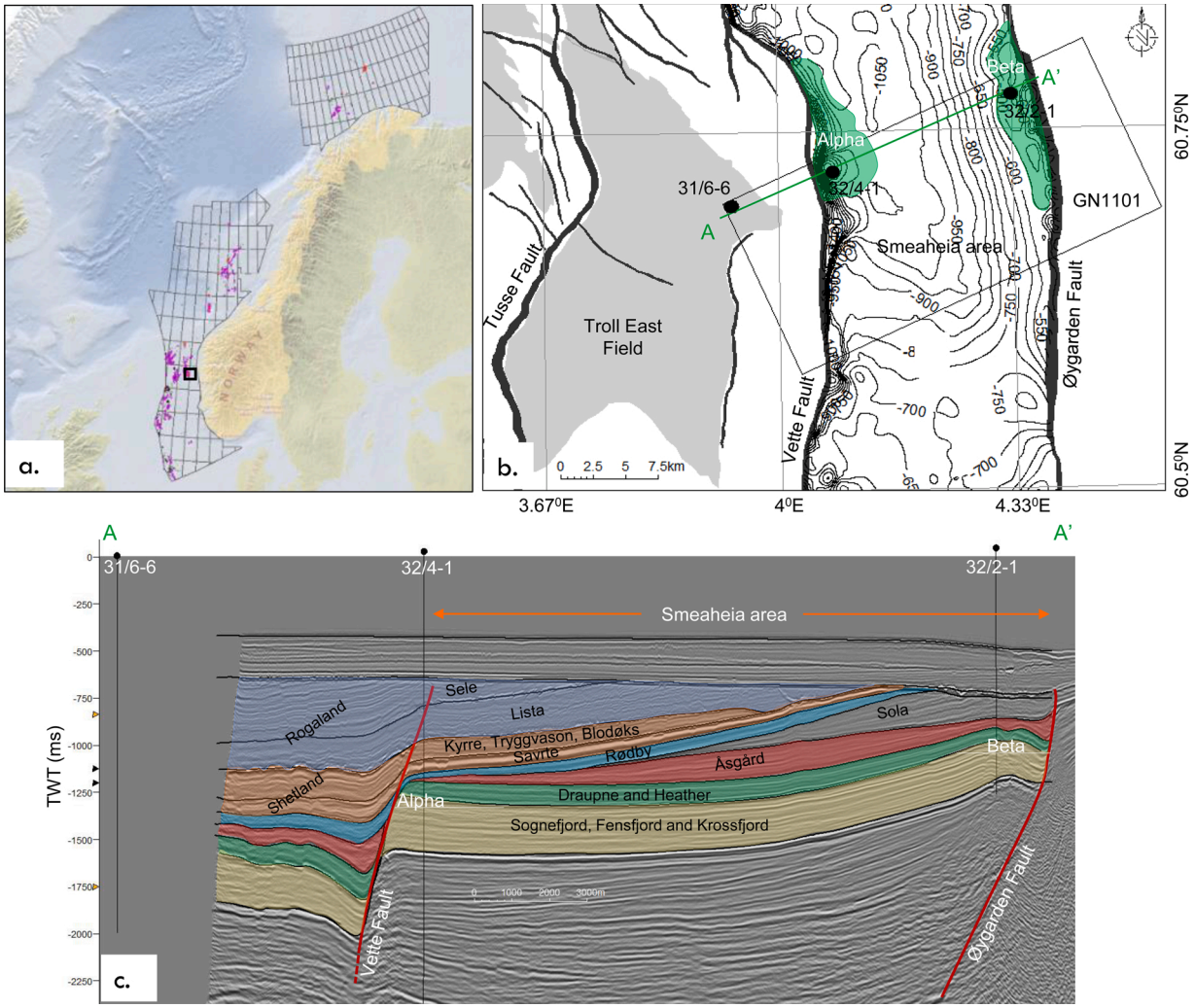

Fig. 1. a) Location (black rectangle) of the study area b) the depth structure map of the top reservoir unit (Sognefjord Formation) is interpreted using the well tops showing the major faults and Troll East Gas Field in the study area, and c) A WSW-ENE seismic profile (AA') crossing three wells shows the faults and critical horizons.

shale smearing throughout the fault zone. However, estimating fault throw using a single fault surface is not representative of the actual scenario because fault zones often contain several major slip surfaces (Childs et al., 1997; Doughty, 2003; Færseth et al., 2007; Foxford et al., 1998; Gibson, 1994; Walsh et al., 1998). Moreover, stress path changes and fault rock strength are not known precisely. Therefore, the deterministic approach assumes that, all the input parameters are well-known with high certainty and that the input consists of only one scenario, which is somewhat questionable when the varying degree of uncertainty exists (Duncan, 2000); instead, obtaining a probability of failure is a more suitable methodology (Christian, 2004; Nadim, 2007).

This study evaluated the stability of Vette fault probabilistically using the Monte-Carlo simulation (MCS) and the First Order Reliability Method (FORM). The fault stability is evaluated using the analytically estimated stress conditions acting on the fault plane and the Mohr-Coulomb failure criteria. The uncertainty of the fault-rock strength properties is handled by interpreting four different fault smearing scenarios and their likelihood based on the study area's geological understanding. The overall VF system reliability is estimated based on the qualitative approximation of all four scenarios using an event tree. The likelihood of each fault rock strength scenario and the corresponding probability of failure is embedded in the system failure number, which could be a reasonable estimation for the future project decision. The pore pressure/stress coupling, also known as the reservoir stress path, is also incorporated to evaluate the complex poroelastic interaction due to the fluid injection in the horizontal stress field. Finally, the relative importance of different parameters (i.e., vertical and horizontal stresses assumptions, pore pressure, stress path, fault rock strength, etc.) on fault stability is evaluated. In the discussion section, we highlighted the potential for a failure probability estimation for subsurface structures. It is a new approach and needs a concrete workflow to implement successfully in the fault stability analysis.

2. Geology of the study area

The Smeaheia area is situated on the northeastern edge of the northern North Sea (i.e., Horda Platform) and bounded by two regional N-S trending normal faults (Fig. 1). The Horda Platform (HP) area experienced two main rifting events during Permo-Triassic and the Late Jurassic to Mid-Cretaceous times (Whipp et al., 2014), where during the 1st rifting event, a wide basin with deep-rooted faults and thick syn-depositional wedges was formed in the center of HP (Stewart et al., 1995). The 2nd rifting event shifted westward but reactivated all the major faults and created a collection of NW-SE trending smaller faults with minor displacement within the proposed reservoir (Sognefjord Formation) and top seal (Heather + Draupne Formations) units throughout the HP (Duffy et al., 2015; Skurtveit et al., 2018; Stewart et al., 1995; Whipp et al., 2014). These events created several N-S trending faults (i.e., Vette, Tusse, Øygarden, etc.), which are believed to be rooted in the Caledonian zones of crustal weakness (Whipp et al., 2014) and tipped out in the overburden stratigraphy into the Rogaland Group (Fig. 1c). The studied Vette fault is one of them which needs to be sealing for safe CO_2 storage in the Alpha structure (Fig. 1b).

The main reservoir rocks in the Alpha structure consist of a succession of three Upper Jurassic sandstone formations (i.e., Sognefjord, Fensfjord & Krossfjord) with good to moderate reservoir quality (Dreyer et al., 2005; Holgate et al., 2015), while organic-rich Heather and Draupne formations act as the primary seal. The reservoir sandstones were deposited in a coastal shallow marine environment and inter-finger with the Heather Formation (Fig. 2a). The Heather Formation shale consists of mainly grey silty claystone with thin streaks of limestone deposited in an open marine environment (NPD, 2020). The organic-rich Draupne Formation shale has an approximate thickness of 106 m in well 32/4-1, which varies laterally and consists of dark grey-brown to black, usually non-calcareous, carbonaceous, occasionally fissile claystone. The Draupne Formation was deposited in an open marine environment with restricted bottom circulation and often anaerobic conditions (NPD, 2020).

The overburden rocks above the Draupne Formation are vital to detect any permeable layer juxtaposition with the reservoirs across the faults. The whole overburden unit is 475–800 m thick, comprising westward-dipping alternating fine- and coarse-grained siliciclastic packages with occasional carbonate-rich deposits (Faleide et al., 2015). The overburden Rødby Formation is crucial as it juxtaposes the top part of the reservoirs. The Rødby Formation consists of red-brown marlstone and deposited in an open marine, oxygenated environment with a

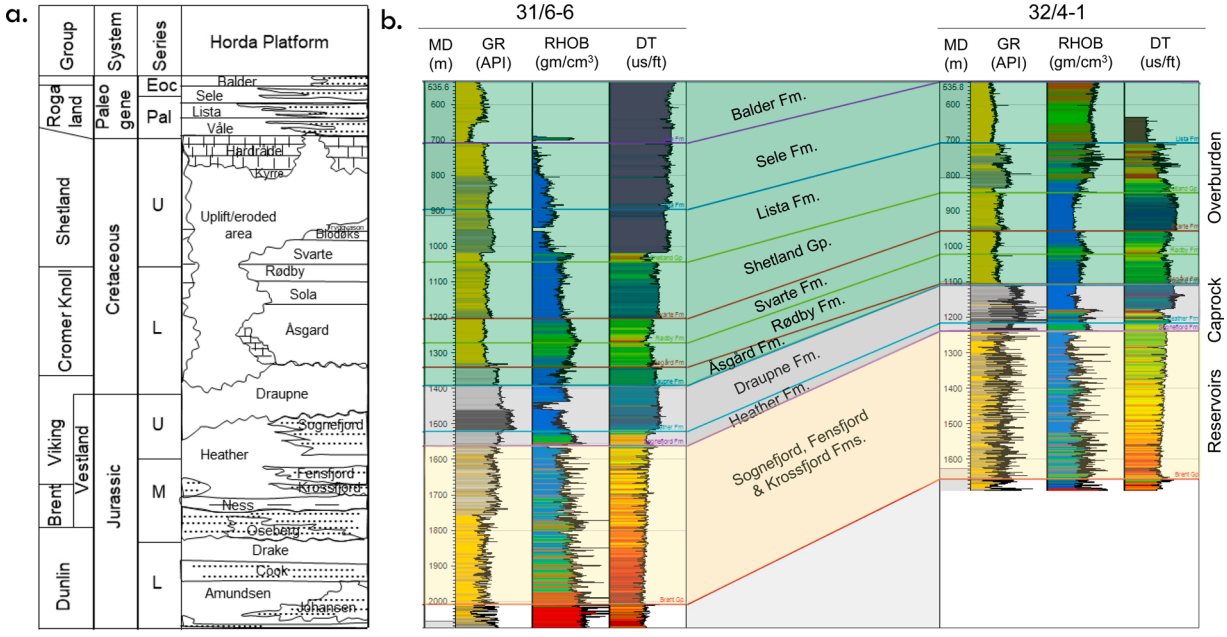

Fig. 2. a) A generalized Jurassic and Cretaceous stratigraphic succession in the study area (modified from NPD CO_2 Atlas, 2014). b) A correlation of footwall (32/4-1) and hanging wall (31/6-6) wells of the Vette Fault flatten on top of Balder Formation. Note the variations in the petrophysical logs (i.e., GR = Gamma-ray; RHOB = Density; DT = Compressional sonic) in both vertical and across the fault direction.

limited supply of clastics (NPD, 2020). In the study area, the Rødby Formation is more calcareous and has a lower gamma-ray response and higher velocity than the overlying units. Wide variations of gamma-ray, density, and P-sonic indicate lithology, acoustic property, and geomechanical changes within the reservoir, cap, and overburden rocks (Fig. 2b).

3. Materials and methods

System reliability of the Vette fault took into account the likelihood of different fault smearing scenarios. The fault stability of each smearing scenario was assessed by an analytically calculated stress acting on the fault plane and the Mohr-Coulomb failure criterion. The workflow used in this study is illustrated in Fig. 3. The input parameters were scouted from the published database (i.e., Gutierrez et al., 2000; Horsrud et al., 1998; Skurtveit et al., 2018, 2015; Zoback, 2010) as well as estimated from the wireline logs from the nearby wells 31/6-6 and 32/4-1. The Mohr-Coulomb failure model that can calculate the Factor of Safety (FoS) was used to define a limit state function of stability. Failure probability was analyzed by the First Order Reliability Method (Hasofer and Lind, 1974) and Monte-Carlo simulation techniques. Finally, the Probability of Failure (P_f) of the Vette fault was estimated for both initial condition and after CO_2 injection scenario for different fault rock strength conditions. The fault system reliability was assessed by combining the likelihood of fault smearing scenarios and the failure probability of each smearing scenario. Moreover, each parameter's sensitivity analysis was investigated by changing one variable at a time while keeping all other input parameters at their initial value (average). In this study, the low and high outcome of the FoS for each uncertain parameter was evaluated.

Most geological processes follow a normal or log-normal law (Christian, 2004). Some geotechnical engineering studies show that changing the probability distribution of the soil parameters from normal to log-normal had a modest effect on the computed probability of failure (Lacasse and Nadim, 1998). Thus, most of the input parameters used for this study were assumed to follow the normal distribution. For the properties that cannot be physically negative within three standard deviations of the average, the distribution is assumed as the log-normal distribution. The standard deviations of the inputs are estimated from the published values.

3.1. Model parameters

3.1.1. Fault smearing scenarios

Fault rock strength is a complicated parameter to describe and highly uncertain; hence it needs a scenario-based approach to deal with the uncertainty. In this study, we evaluated all possible fault zone rock smearing scenarios within the Vette fault employing the interpretation of 3D seismic data of GN1101 (Fig. 4). The major and minor faults with horizons were interpreted from seismic to evaluate the possible fault-rock setup. The reservoir intervals (i.e., Sognefjord, Fensfjord, and Krossfjord formations) in the footwall side juxtapose with the Cromer Knoll Group (i.e., Rødby and Åsgard formations) in the hanging wall side in the Alpha prospect (Fig. 4a). Three possible shale smearing scenarios were interpreted in the studied Vette fault region (Fig. 4b–d). The most likely scenario was the Rødby Formation smearing case. The upper part of the reservoir unit (i.e., Sognefjord Formation) has the best quality reservoir properties (i.e., high porosity and permeability); hence, CO_2 plume is likely to migrate and accumulate within this zone. The Sognefjord Formation is juxtaposed with the Rødby Formation with a minimal fault throw (Færseth et al., 2006), making this formation the best possible smearing candidate (Fig. 4b). Åsgard Formation that pinches out near the fault's footwall side is least likely to be smearing (Fig. 4c); hence we excluded that from the smearing scenario cases. The shale smearing of the primary caprocks (i.e., Draupne and Heather formations) is also very uncertain as the fault throw is significantly large (~1500 m)(Fig. 4d). According to Færseth et al. (2006), the chances of smearing are reduced with increasing fault throw. In this study, the qualitative clay smearing scenarios are evaluated; however, the quantitative SGR values are not estimated. One can not rule out the presence of reservoir rock (i.e., Sognefjord Formation) fragments within the fault zone, which can be considered another fault rock strength scenario (Skurtveit et al., 2018).

Considering the seismic interpreted clay smearing (Fig. 4) and reservoir fragment scenarios with a typical static friction fault without cohesion (Zoback, 2010), we recognized four possible scenarios to analyze for the probability of failure estimation (Table 1). The qualitative probability of each condition was also assigned based on the geological interpretation. Moreover, the probabilistic likelihood values for each scenario were estimated based on the geological understanding of each case, which was later used to quantify the Vette Fault system reliability. Seismic interpretation-related uncertainties (i.e., human error, seismic quality, sub-seismic fault plane, etc.) are always present (Bond et al., 2015), but these are out of the scope of this research. However, the proposed event tree method considered all the uncertainties to estimate the system failure value.

3.1.2. In-situ stress condition

The present-day stress conditions (i.e., vertical and horizontal stresses) on top of the reservoir (i.e., top Sognefjord Formation) were both scouted (i.e., Skurtveit et al., 2018; Statoil Underground report, 2016) and estimated using wireline logs. The vertical stress (σ_v) was calculated using the average density obtained from the density log (Fig. 5) in well 32/4-1. Later the published and estimated vertical stresses were averaged and used for the analysis (Table 2). The initial horizontal stress and pore pressure were both calculated from the XLOT data (Fig. 6) and directly used from the reference data analyzed by Skurtveit et al. (2018). The σ_v was estimated using the following equation:

$$\sigma_v = \rho_f h_w g + \rho_b h_o g \quad (1)$$

where, ρ_f is saline water density (~1025 kg/m^3), h_w is the water depth (~312 m), ρ_b is the bulk density (average) of the overburden formations (~2233 kg/m^3), h_o is the thickness of the overburden (~902 m), and g is the gravitational acceleration. The average bulk density used in this study was obtained by integrating the whole overburden. The estimated point data, using the average density, was later used with scouted vertical stresses to evaluate the range (Table 2).

According to Skurtveit et al. (2018), a normal faulting regime (i.e., vertical stress is greater than horizontal stresses) with isotropic horizontal stress conditions (i.e., maximum horizontal stress = minimum horizontal stress) is a reasonable stress model for the study area. The extended leak-off test (XLOT) data from the nearby Troll area also

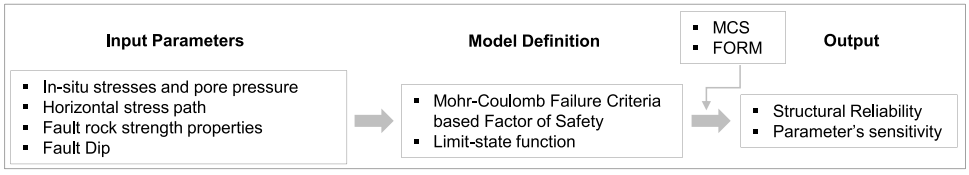

Fig. 3. The workflow to estimate the failure probability of the Vette Fault, used in this study.

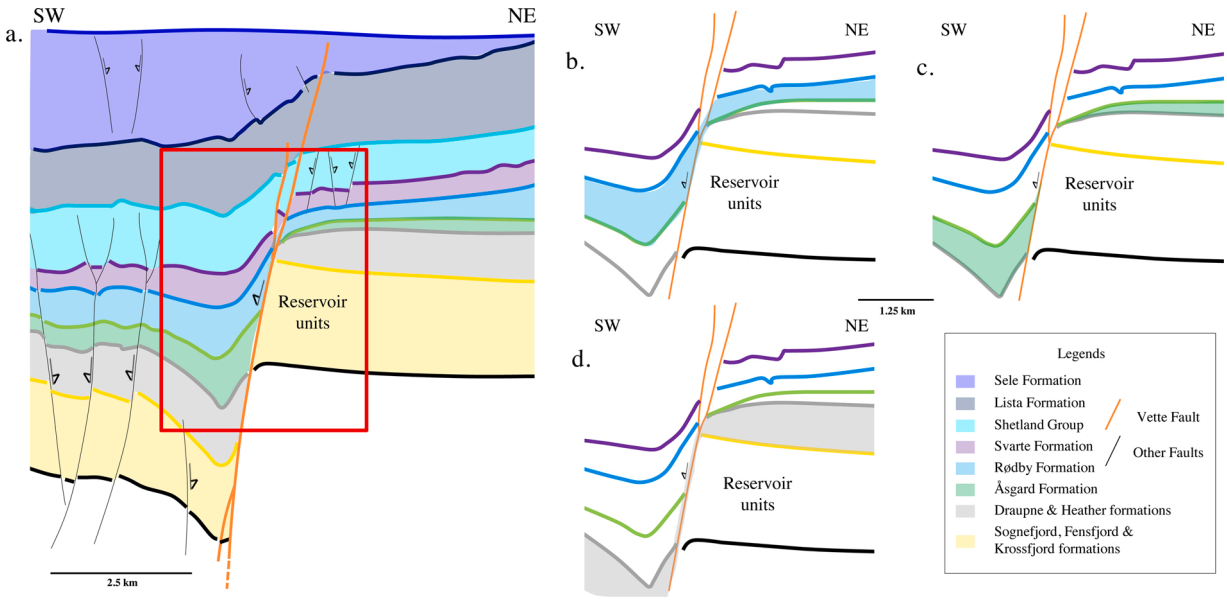

Fig. 4. a) Schematic representation shows the seismic interpretation of horizons and faults. The zone of interest (red rectangle) is further analyzed for possible shale smearing along the Vette fault zone for, b) Rødby Formation, c) Åsgard Formation, and d) Draupne and Heather formations.

Table 1
Possible fault smearing scenarios and likelihoods based on the geological explanation. Note that the likelihood terms are taken from Nadim (2007).

	Fault Smearing Scenario	Likehood	Probability Range[a]	Assign Probability[b]
Case 1	Static frictional fault	Very Unlikely	0 – 0.1	0.01
Case 2	Sognefjord rock fragment	Unlikely	0.1 – 0.25	0.12
Case 3	Draupne smearing	Unlikely	0.1 – 0.25	0.07
Case 4	Rødby smearing	Likely	0.5 – 0.9	0.80

[a] Based on Nadim (2007) and Brændeland et al. (2010).
[b] Based on Geological understanding of Vette fault.

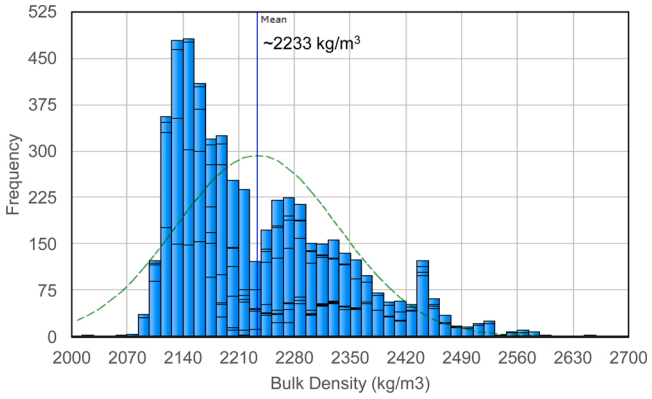

Fig. 5. Distribution of bulk density log of overburden formations of well 32/4-1. The mean density value for the overburden is 2233 kg/m^3.

revealed that the Alpha structure is within the normal faulting regime because the vertical stress gradient is significantly higher than the horizontal stress profile (Fig. 6). The hydrostatic pore pressure gradient was calculated using the depth profile from the well 32/4-1.

The post-injection scenarios assume a pore pressure change of 0.82 MPa by CO_2 injection, which was used from the Statoil dynamic simulation model analyzed for the Smeaheia feasibility study (Gassnova, 2016). The model used an injection rate of 1.3 MT per year over a period of 25 years within an excellent quality (permeability 1.3D, porosity 35 %, and thickness 60 m) reservoir (i.e., Sognefjord Formation). The compaction-induced changes in the total vertical stress were minimal for laterally extensive reservoirs, assuming equal elastic properties for the reservoir and the overburden (Geertsma, 1973). Moreover, the stiffness contrast of factor 10 in a numerical model shows a very negligible effect on the vertical total stress change in a laterally extensive reservoir (Hettema et al., 2000). The main reservoir rock (Sognefjord Formation) in the study area is also laterally extensive, which indicated an insignificant vertical stress change due to pore pressure variation; hence we do not consider any vertical stress changes in our model. The change of the effective vertical stress was thus assumed to be the same as pore pressure. However, the horizontal stress path, which is sensitive to the pore pressure changes, was calculated from the log-based Poisson's ratio using the equation proposed by Hettema et al. (2000):

$$\gamma_h = \frac{\Delta\sigma_h}{\Delta P} = \alpha\left(\frac{1-2\nu}{1-\nu}\right) \tag{2}$$

where σ_h is the total horizontal stress; ΔP is the pore pressure change; α is Biot's coefficient, and ν is the Poisson's ratio.

Moreover, fault can influence the horizontal stress changes during injection if major faults bound the reservoirs, or the injection points are near the fault (Addis et al., 1998, 1994). Therefore, the total horizontal stress in a normal faulting region was also estimated, which can be written as:

$$\gamma_{fault} = \alpha\left(\frac{2\sin\psi}{1-\sin\psi}\right) \tag{3}$$

where $\nu \geq (1-\sin\psi)/2$, with ψ being the fault friction angle. If $\nu < (1-\sin\psi)/2$, the minimum horizontal stress re-orientates parallel to the strike of the fault, and the stress path becomes:

$$\gamma_{fault} = \alpha\left(\frac{\sin\psi + 1 - 2\nu}{1+\sin\psi}\right) \tag{4}$$

3.1.3. *Fault rock geometry and strength*

The fault rock geometry significantly changes with changing horizontal and vertical directions. Therefore, in this study, we estimated the

Table 2
The database used in this study with the type of distribution and data sources.

Parameters	Average	Unit	Standard Deviation	Random Distribution	Sources
Initial vertical stress (σ_v)	22.25	MPa	0.65	Normal	Skurtveit et al., 2018; Wireline log (RHOB; Eq. (1))
Initial horizontal stress (σ_h)	16.85	MPa	0.95	Normal	Skurtveit et al., 2018; XLOT
Initial pore pressure (Pp)	10.48	MPa	1.32	Normal	Skurtveit et al., 2018; XLOT
Horizontal stress path (γ_h)	0.51	–	0.07	Normal	Wireline log (PR; Eq. (2))
Horizontal stress path (γ_{fault})	0.54	–	0.03	Normal	Wireline log (PR; Eq. (4))
Vette fault Dip (θ)	45.25	Degree	4.00	Normal	Fault surface interpreted from 3D seismic in zone of interest
Friction angle, cohesionless (ϕ^1)	31.00	Degree	0.00	–	Standard cohesionless fault angle (Zoback, 2010)
Cohesion, Sognefjord (S_0^2)	5.01	MPa	1.62	Log-Normal	Skurtveit et al., 2018; Wireline log (PHIT; Eq. (5))
Friction angle, Sognefjord (ϕ^2)	19.50	Degree	4.50	Normal	Skurtveit et al., 2018
Cohesion, Draupne (S_0^3)	3.93	MPa	1.05	Log-Normal	Skurtveit et al., 2015; Horsrud et al., 1998; Gutierrez et al., 2000; Wireline log (DT; Eq. (6))
Friction angle, Draupne (ϕ^3)	21.63	Degree	5.14	Normal	Skurtveit et al., 2015; Gutierrez et al., 2000
Cohesion, Rødby (S_0^4)	6.81	MPa	0.60	Log-Normal	Wireline log (DT; Eq. (6))
Friction angle, Rødby (ϕ^4)	21.63	Degree	5.14	Normal	Equivalent to Draupne

MPa – Mega Pascal; The numbers shown as superscript in the friction angle and cohesion are indicated case numbers mentioned in Table 1.

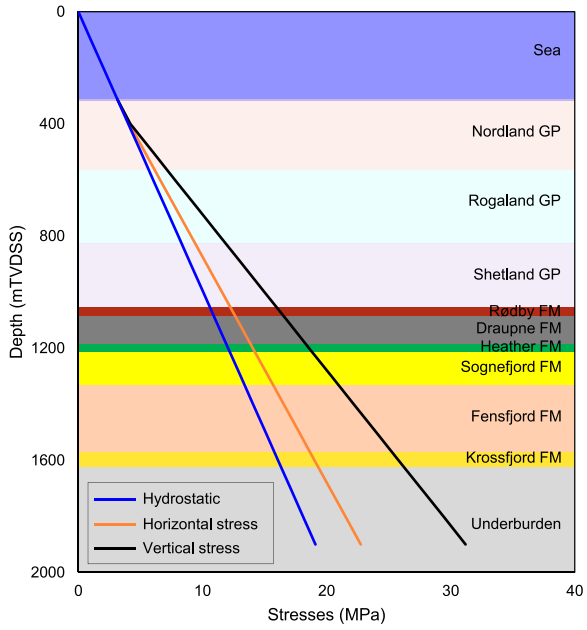

Fig. 6. In-situ stress profile for the Alpha structure assuming normal faulting regime with isotropic horizontal stress condition. Note that the vertical and horizontal stress profiles were calculated using extended leak-off test (XLOT) data from the nearby Troll area. The hydrostatic profile was estimated using water density ~1025 kg/m^3.

fault dip within the zone of interest (from the top of Rødby Formation to the base Viking Group), because the CO_2 injection-related impact will be encountered in this zone. The average dip of the fault in the zone of interest is calculated by the fault interpretation module in the Petrel-2018 software using the available 3D seismic data (i.e., GN1101), where the mean value is estimated at 45.25° from the 3D interpretation of the Vette fault.

Rock strength parameters (i.e., cohesion and friction angle) for case 2 (Sognefjord equivalent) and case 3 (Draupne equivalent) were available from laboratory test results (Gutierrez et al., 2000; Horsrud et al., 1998; Skurtveit et al., 2018, 2015). However, there was no laboratory-measured data for Rødby Formation (Case 4). Therefore, the empirical equations based on porosity (for Sandstone) and P-wave velocity (for shale) were used to estimate the uniaxial compressive strength (C_0) for all different scenarios. In cases 2 and 3, both laboratory test data and empirically estimated data are averaged and used as input parameters, whereas for case 4, the only option is the estimated data.

The empirical equation used for case 2 is taken from Plumb (1994), which stated that:

$$C_0 = 357(1 - 2.8\Phi)^2 \ (\Phi < 0.357) \quad (5)$$

where C_0 is in MPa and Φ as a fraction

And Horsrud (2001) equation was used for cases 3 and 4:

$$C_0 = 0.77V_p^{2.93} \ (\Phi = 30 - 55\%) \quad (6)$$

where C_0 is in MPa and V_p is in km/s

Moreover, the same average friction angle is used for both cases 3 and 4 as there are no measurements for Rødby Formation.

The Mohr-Columb plot of the initial stress state condition on top of the reservoir near the Vette fault is shown in Fig. 7. The Columb failure surfaces for all the fault rock strength scenarios are also representing the relative distance from the Mohr circle. Moreover, the fault plane dipping points (red points) on the Mohr-Columb diagram show that the fault dipping close to 60° is the closest to the classical fault failure surface compared with 45°. In this study, the mean Vette fault dip interpreted in the zone of interest is 45.25°. However, overall, the fault plane dip ranges from 35 to 52°.

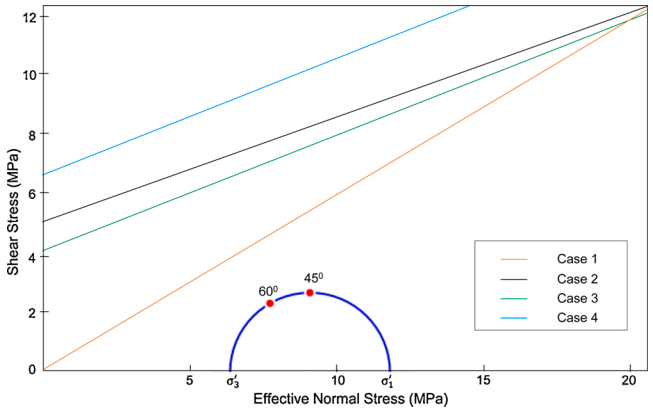

Fig. 7. The Mohr-Columb plot is representing the shear stress and effective normal stresses of the initial reservoir stress state condition. The failure surfaces for all the fault rock strength scenarios (Table 1) are shown for comparison. Note that red points on top of the Mohr circle represent the fault plane location based on the fault dip.

3.2. Model definition

3.2.1. Reliability analysis concept

The reliability analyses provide a rational framework for dealing with the structural uncertainties that assist in making the decision. However, the probability of failure does not necessarily correspond to high safety (deterministic estimation); instead, it depends on the uncertainties in load and resistance (Nadim, 2007). For a structural component with uncertain resistance R and load S and their random variables, probability density functions $f_R(r)$ and $f_S(s)$ respectively, the probability of failure may be determined by:

$$P_f = P(R \le S) = P(R - S \le 0) = \int_{-\infty}^{\infty} f_R(X) f_S(X) dx \tag{7}$$

where X is the random variable, assuming the load and the resistance variables are statistically independent.

However, the probability of failure is not determined by the overlapping of the two curves but by the realization of the random variables R and S. If both the resistance and load variables are normally distributed, the failure probability may be assessed directly by considering the random variable M often referred to as the safety margin:

$$M = R - S \tag{8}$$

where the probability of failure may be assessed through

$$P_f = P(R - S \le 0) = P(M \le 0) \tag{9}$$

where M is also normally distributed with parameters with the mean $\mu_M = \mu_R - \mu_S$ and standard deviation $\sigma_M = \sqrt{\sigma_R^2 + \sigma_S^2}$.

The failure probability may be determined by the use of the standard normal distribution function as:

$$P_f = \Phi\left(\frac{0 - \mu_M}{\sigma_M}\right) = \Phi(-\beta) \tag{10}$$

where $\mu_M/\sigma_M = \beta$ is called the safety/reliability index, which is the standard deviation by which the mean value of the safety margin M exceeds zero or most likely exceeds the failure point (Fig. 8).

However, if the resistance and the load cannot be described by only two random variables but rather by functions of the same random variables and statistically dependent, the safety margin M will be:

$$M = R - S = f_1(X) - f_2(X) = g(X) \tag{11}$$

where X is a vector with n so-called basic random variables, the function g(X) is denoted as the limit state function, which is a boundary between desired (g(X) >0) and undesired (g(X) ≤ 0) performance of any structure and defined within a mathematical model for functionality and performance (Ditlevsen and Madsen, 2007).

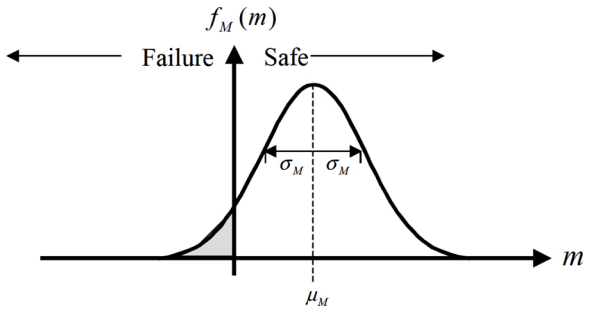

Fig. 8. Normally distributed, the probability distribution function of safety margin M showing the probable failure and safe zones (adapted from Faber, 2009).

3.2.2. Limit state function

In this study, we considered the limit state function is based on the Mohr-Coulomb failure criteria. Considering isotropic horizontal stress condition and normal faulting regime in the study area (Skurtveit et al., 2018), the factor of safety (FoS) is defined as:

$$FoS = \frac{\tau_{MC}}{\tau_{current}} \tag{12}$$

$$\tau_{MC} = S_0 + \sigma_n^{'} \cdot tan\varnothing \tag{13}$$

$$\tau_{current} = \frac{\sigma_1^{'} - \sigma_3^{'}}{2} \cdot sin2\theta \tag{14}$$

$$\sigma_n^{'} = \frac{\sigma_1^{'} + \sigma_3^{'}}{2} + \frac{\sigma_1^{'} - \sigma_3^{'}}{2} \cdot cos2\theta \tag{15}$$

where τ_{MC} is critical shear stress or shear strength, $\sigma_n^{'}$ is effective normal stress, S_0 is cohesion, σ_1 is initial vertical stress, σ_3 is initial horizontal stress, $\sigma_1^{'}$ is effective vertical stress, $\sigma_3^{'}$ is effective horizontal stress, $\varnothing$ is an effective friction angle, and θ is fault dip.

The state of the structure is safe when the factor of safety is greater than 1 and fails when it is less than 1. Therefore, the limit-state function defines as:

$$g(x) = FoS - 1 \tag{16}$$

where g(x) is the limit-state function which is the boundary between safe (g(x) >0) and failure (g(x) ≤ 0) state.

3.3. Reliability method

Several well-established reliability methods are available (i.e., First Order Second Moment, First Order Reliability Method/Second Order Reliability Method, Monte Carlo simulation, etc.). We tested Monte Carlo Simulation (MCS) and First Order Reliability Method (FORM) to estimate Vette fault's probability of failure. The MCS is a procedure where the limit state function is evaluated by randomly selected samples from the input values to determine whether the configuration is desirable or not. The probability of failure (P_f), however, is estimated by the number of unwanted settings (n_f), with respect to the total numbers of samples (n).

$$P_f = \frac{n_f}{n} \tag{17}$$

It is a powerful technique but sometimes impractical when the probability of failure is small and requires many simulations to obtain a reliable distribution. However, sampling techniques (i.e., Latin Hypercube, Orthogonal, etc.) can optimize the number of simulations required for reliable distribution of the response, which we did not consider in this study.

On the contrary, the First Order Reliability Method (FORM) is a basic method for reliability evaluation in structural reliability theory and is widely used in practical engineering problems (Faber, 2009; Nadim, 2007), which is proposed by Hasofer and Lind (1974). According to this method, the reliability index (β_{HL}) is the shortest distance z* from the origin to the failure surface g(z) in a normalized space and denoted as:

$$\beta_{HL} := \beta = \overrightarrow{\alpha^T} z^* \tag{18}$$

where the normalized space is transformed to standardized normally distributed random variables with zero means and unit standard deviations (Fig. 9). $\overrightarrow{\alpha}$ denotes the normal vector to the failure surface g(z) and is given by:

$$\overrightarrow{\alpha} = -\frac{\nabla g(z^*)}{|\nabla g(z^*)|} \tag{19}$$

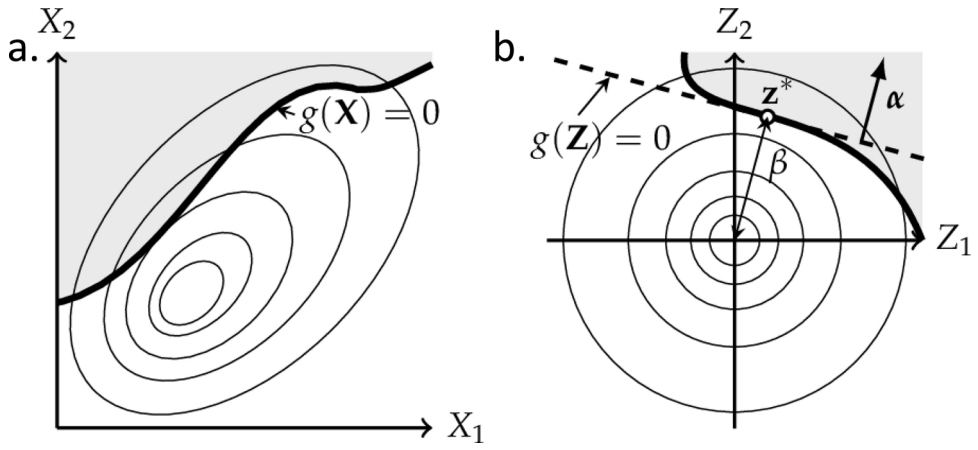

Fig. 9. a) Illustration of a physical space of two random variables (X1 and X2) with the limit state function stated g(X), and b) after normalization of the random variables into standardized normally distributed variables Z with the design point z* and reliability index β. Note that the grey shaded area denoted the failure domain, and g(X)/g(Z) = 0 is the failure surface (modified after Madsen et al., 2006).

where g(z) is the gradient vector, which is assumed to exist:

$$\nabla g(z) = \left(\frac{\partial g}{\partial z_1}(z), \ldots\ldots\ldots, \frac{\partial g}{\partial z_n}(z)\right) \tag{20}$$

Therefore, the reliability index β is an optimization problem and non-linear case; an iterative method must be used (Madsen et al., 2006; Thoft-Christensen and Baker, 1982). Hence the probability of failure is equal to the probability that an undesired performance will occur and determined through the following n-dimensional integral:

$$P_f = \int_{g(x)\leq 0} f_X(X)dx \tag{21}$$

where $f_X(X)$ is the joint probability density function for the vector of basic random variables X, and the integration is performed over the failure domain. This procedure called FORM, and β is the First Order Reliability Index (Madsen et al., 2006). The results of FORM, which uses a linearization of the limit state function, could be inaccurate if the points for the linearization are not properly selected. This study adopted a search algorithm to find the most probable failure points instead of using the mean and the standard deviation as the linearization points.

The Python-based open-source structural reliability analysis module PyRe (Hackl, 2018) was used to initiate and run the MCS and FORM techniques models. PyRe has been created from FERUM (Finite Element Reliability Using Matlab) project started in 1999 at the University of California, Berkeley, for pedagogical purposes. However, only the core function of the FERUM was implemented, which focuses on the reliability analysis and not considered finite element methods. Along with the core reliability functionality and summarizing output, PyRe is also very flexible and extensive, making it applicable to a large suite of problems. Other softwares, such as excel™ 2016 version is used for the cross-plots and sensitivity analysis, while 2018 version of Petrel™is used for seismic and petrophysical interpretation. Moreover, the MohrPlotter™ version-3 is used for the Mohr-Columb failure plot.

4. Results

4.1. Estimated reliability of the Vette fault

The probability of failure of the Vette fault is summarized in Table 3. All four different fault smearing scenarios described in chapter 3.1.1 are considered for this reliability analysis. As outlined in Table 3, the probability of failure (P_f) of the Vette fault varies significantly with the variation of fault rock strength properties (i.e., different cases). When the fault smearing is assumed as cohesionless material (i.e., case 1), this scenario results in the highest probability of failure (i.e., 1.64E-02). However, when the fault smearing scenario is assumed to be from Rødby Formation (i.e., case 4), the calculated probability of failure (i.e., $<10^{-6}$) using the number of trials 10^8. The failure probability of cases 2 and 3 ranges in between at 10^{-4} and 10^{-6}, respectively.

Table 3
Probability of failure of VF in different scenarios estimated using MCS and FORM.

	Monte-Carlo		FORM	
	Initial condition	After injection	Initial condition	After injection
Case 1	1.64E-02	1.24E-02	8.70E-03	1.16E-02
Case 2	1.14E-04	1.15E-04	1.68E-04	1.27E-04
Case 3	7.58E-06	8.60E-06	2.84E-04	2.01E-04
Case 4	$<10^{-6}$	$<10^{-6}$	1.20E-11	2.23E-12

The MCS results are sensitive to the number of trails; hence, the accuracy depends on it. If there are enough trials, the MCS calculates fairly accurate probability. The number of MCS trial sensitivity is shown in Fig. 10, where failure probability is run in different iterations for case 1 initial scenario. The obtained failure probability fluctuated significantly and eventually became insensitive to the number of trials when the number was larger than 10^6. This indicated that the probability of failure estimated using MCS for cases 3 and 4 are within the sensitive zone and need additional trials for more accurate values.

On the contrary, the First Order Reliability Method (FORM) gives

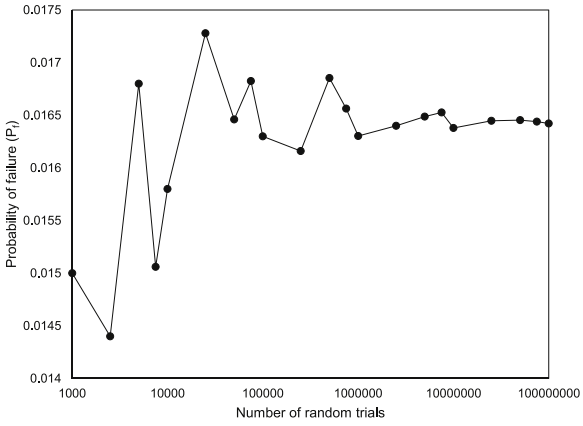

Fig. 10. Failure probabilities were calculated based on the different number of iterations for case 1, showing the sensitivity of the MCS method.

consistent failure results compared with the MCS (i.e., cases 1 and 2) (Table 3). As cases 3 and 4 need more trials in the MCS method, we assume FORM approximated realistic values for these cases. Therefore, FORM results in this study are considered reliable and used for further discussions.

When the FORM results are compared with the initial condition, and after CO_2 injection scenarios, the difference is minimal. Although the pore pressure change due to injection is used as a deterministic number in this study, the after-injection scenarios showed a slightly higher failure value than the initial condition except case 4, where the value is somewhat smaller (Table 4). The reliability index value in the First Order Reliability Method also followed a similar trend (i.e., lower in the after-injection scenarios than the initial condition except case 4).

The differences in fault failure for horizontal stress path calculated using Eqs. (2) and (4) are very minimal. The P_f values using the FORM method in the after-injection scenario are shown in Table 5. Overall, the normal faulting region horizontal stress change option has slightly lower values compared to the case where we ignored the faulting influence.

4.2. Computational efficiency

The concepts of both stochastic Monte-Carlo simulation and the First Order Reliability Method are different and have their advantages and disadvantages. Monte-Carlo simulation is a powerful technique, but analyzing a very low (i.e., case 4) structural probability of failure can sometimes be unrealistic. For example, to estimate the case 4 failure probability, the Monte-Carlo simulation required more than 10^{12} trials (FORM estimated failure value is 2.23E-12), which are very time-consuming and practically impossible. In contrast, the number of iterations needed to approximate the reliability index in the First Order Reliability Method is minimal (Table 6); hence, the time required is insignificant but shown to be quite accurate compared to Monte-Carlo simulation results.

4.3. Sensitivity analysis

Both deterministic and probabilistic sensitivity factors are evaluated where each has its unique advantages. The deterministic sensitivity indicates how much each random variable's mean and standard deviation contributes to the response's variability. In contrast, the probabilistic sensitivity, which results from the probabilistic analyses, indicated each parameter's effect on the reliability function (Easley et al., 2007).

4.3.1. Deterministic sensitivity

Each parameter's weight acted on the Vette fault safety factor is analyzed using 'one variable at a time' (OVAT) sensitivity analysis technique (Campolongo et al., 2000; Rohmer and Seyedi, 2010). The concept is that each input parameter is alternatively assigned its minimum and maximum values, whereas the other input parameters are fixed to their mean values. The input parameter ranges are summarized in Table 7. The factor of safety parameter has been calculated as output using Eq. (12). The case 4 scenarios are illustrated here as equivalent to the Rødby Formation strength case, which is most likely the scenario based on our geological interpretation.

The OVAT analysis illustrated that the initial horizontal and vertical stresses (i.e., initial stress state) have the most significant impact than any other input parameters (Fig. 11). Therefore, these can be the critical parameters related to the fault failure risk. The smallest value of $\sigma_3^{'}$ corresponds to the highest failure tendency and vice versa. On the contrary, the minimum value of $\sigma_v^{'}$ denotes the higher safety state while the higher failure state symbolizes the maximum $\sigma_v^{'}$ values. The fault rock strength properties (i.e., cohesion and friction angle) and pore pressure also have a strong influence on safety measures. On the contrary, the horizontal stress path and fault dip values have minimal effect on assessing fault safety.

4.3.2. Probabilistic sensitivity

The relative design sensitivity factors or the relative importance factors (α) are often referred to as probabilistic sensitivity factors, which are very useful for the relative ranking of random variables. This is obtained by performing several probabilistic analyses and treating every individual parameter as a deterministic variable in each study (NESUS Theoretical Manual, 2011; Pereira et al., 2014). A positive sensitivity indicates a direct relationship between the variable's value and the response, while a negative sensitivity suggests an inverse relationship. Moreover, the square of each sensitivity factor (α_i^2) is a measure of its contribution to the probability, and the sum is equal to unity (i.e., 1). However, this sensitivity factor is not always ideal for the design process as it is only represented by standard normal variates while the mean, standard deviation, and distribution type needed to represent the full picture (Easley et al., 2007).

In this study, the probabilistic sensitivity factors (α) showed that different variables' relative significance is different in other cases (Fig. 12). For example, in case 1, pore pressure (P_p) and horizontal stress (σ_h) contributed most of the variability, while the fault dip (θ) with the null value indicated no contribution. In contrast, horizontal stress (σ_h), fault dip (θ), and cohesion (S_0) represent the most contributor

Table 4
Probability of Failure (P_f) and Reliability Index (β) of different scenarios estimated using FORM in the initial condition and after injection scenarios.

	Initial condition		After injection	
	P_f	β	P_f	β
Case 1	8.70E-03	2.3781	1.16E-02	2.2692
Case 2	1.68E-04	3.5856	1.27E-04	3.6586
Case 3	2.84E-04	3.4465	2.01E-04	3.5384
Case 4	1.20E-11	6.6797	2.23E-12	6.9219

Table 5
Effect of injection-related horizontal stress path on failure probability values estimated using FORM.

	γ_h	γ_{fault}
Case 1	**1.16E-02**	**1.16E-02**
Case 2	**1.27E-04**	**1.20E-04**
Case 3	**2.01E-04**	**2.01E-04**
Case 4	**2.23E-12**	**2.23E-12**

Table 6
The number of iterations to estimate the failure probability represents the time required for each technique.

	FORM[a]	Monte-Carlo
Case 1	**6**	100000000
Case 2	**9**	
Case 3	**10**	
Case 4	**26**	

[a] The number of iteration required to minimize the distance to the design point z in the Eq. (20) from origin.

Table 7
Input parameters with minimum and maximum values used in the deterministic sensitivity analysis.

Parameter	Value Range
Initial vertical stress (σ_v)	**21.60−22.90 (MPa)**
Initial horizontal stress (σ_h)	**15.90−17.80 (MPa)**
Pore pressure (Pp)	**9.16−11.80 (MPa)**
Horizontal stress path (γ_h)	**0.44−0.58**
Vette fault Dip (θ)	**41.25–49.25°**
Cohesion, Rødby (S_0)	**6.21–7.41 (MPa)**
Friction angle, Rødby (ϕ)	**16.49−26.77°**

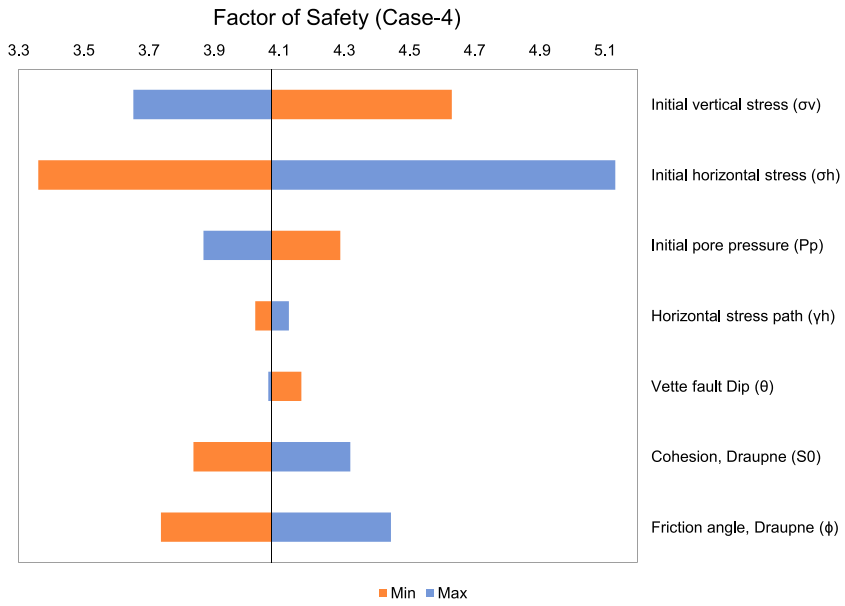

Fig. 11. The tornado diagram of the most likely scenario (case 4) after the injection case shows the relative importance of parameters.

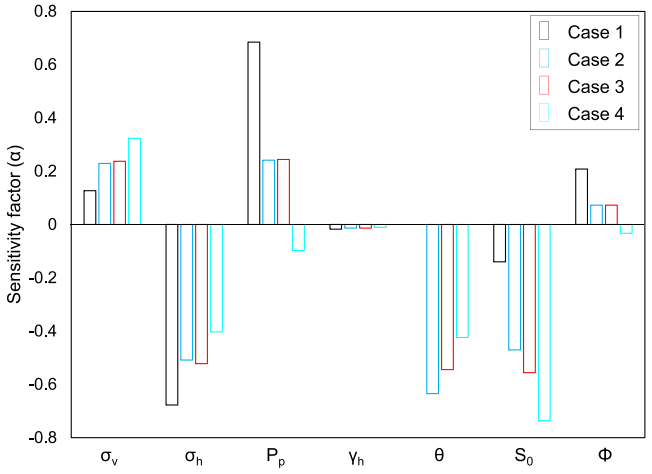

Fig. 12. Sensitivity factors (α) for the probabilistic analysis of Vette fault using FORM showing the relative ranking of the random variables (i.e., σ_v = Vertical stress; σ_h = Horizontal stress; P_p = Pore pressure; γ_h = Horizontal stress path; θ = Fault dip; S_0 = Cohesion and Φ = friction angle).

parameters for the rest of the cases (i.e., cases 2, 3, and 4). The least influential factor for all the cases is the horizontal stress path (γ_h), which is also shown in deterministic sensitivity analysis for case 4 (Fig. 11). Overall, both analyses for case 4 have similarities except fault dip (θ) and friction angle (S_0), where a significant variation was observed between the analyses.

4.4. System reliability analysis of Vette fault

In this study, we estimated the Vette fault system reliability using an event tree. The reliability results of each case show that the most unlikely scenario (i.e., case 1) resulted in a 100 times higher probability of failure than less likely scenarios (i.e., cases 2 and 3) and a million times higher probability than likely scenarios (i.e., case 4). To evaluate the overall stability of faults, the probability of possible fault smearing cases is weighted by scenario likelihoods. The event probability values for each likelihood are assigned based on the Vette fault's geological understanding, while the ranges are validated using the published literature (Brændeland et al., 2010; Nadim, 2007). Subsequently, for each case, the failure and non-failure state are estimated using the probability of failure values calculated by the FORM. We used the FORM estimated P_f values because all the fault rock strength scenarios have approximated values that are quite accurate compared to the Monte-Carlo simulation results in higher P_f scenarios (i.e., case 1 and 2). The total probability of failure and non-failure values for each case are estimated by considering the fault rock strength parameters (i.e., cohesion and friction angles) uncertainties. Finally, by adding all the failure values, the system failure of the Vette fault is calculated.

The calculated system reliability is summarized in Fig. 13. The computed system probability of failure of the Vette fault is around 1.46E-04. The Vette fault system failure values are equivalent to cases 2 and 3 (i.e., 1.27E-04 and 2.01E04, respectively) while significantly higher than case 4 (i.e., 2.23E-12) and lower than case 1 (i.e., 1.16E-02). Although case 1 is a very unlikely scenario, this scenario's weight on system failure's total probability is important (i.e., 1.16E-04 out of 1.46E-04), because the probability of failure of scenario 1 is significantly higher than the other scenarios. On the contrary, the contribution of the most likely scenario (i.e., case 4), which has the probability of failure of 10^{-12}, on the total system failure probability seems to be negligible. If we exclude the unlikely scenarios from the decision making, it can underestimate the system failure. Thus, caution needs to be taken for the low likelihood scenarios; for example, in the worst-case scenario (i.e., case 1), the consequences might be intense. The event tree is used to calculate system failure probability, which considered all the probabilistic incident, hence an excellent approach to represent the system reliability.

The system reliability index (β) is also estimated from the relationship between the probability of failure (P_f) and the reliability index (β). The trend line is drawn using the data points calculated for different cases in the initial condition scenario using the FORM. According to the graph, the Vette fault system reliability is ~3.7 (Fig. 14).

5. Discussion

In the case of Vette fault stability in the Smeaheia area, the failure probability estimation approach is new and essential to understanding the fault seal risks. The riskiest scenario (i.e., case 1) is unlikely to happen as several similar fault-related traps (i.e., Tusse, Svartalv, and Troll faults) in nearby Troll Field contain thick hydrocarbon columns.

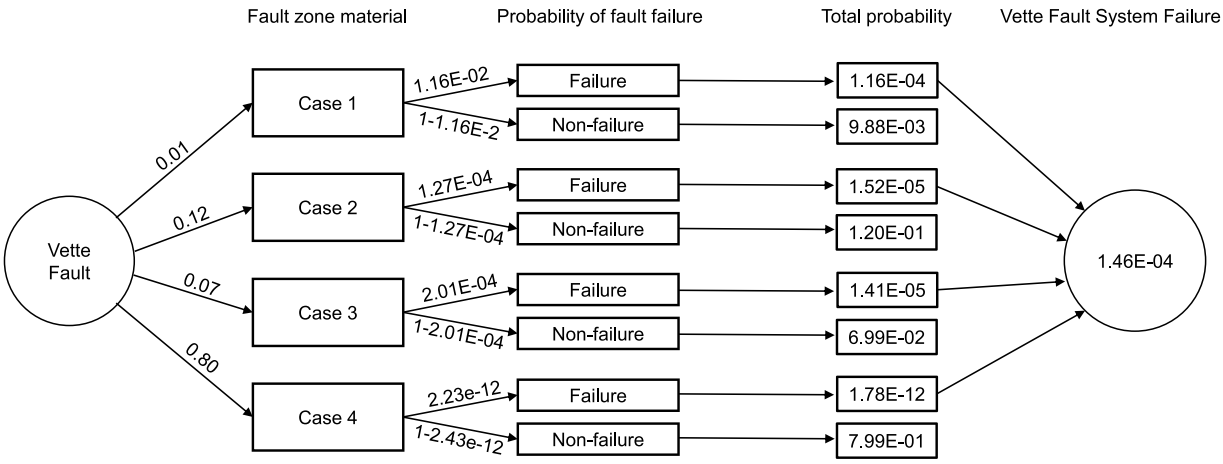

Fig. 13. Event tree of Vette fault system reliability analysis showing the system failure number.

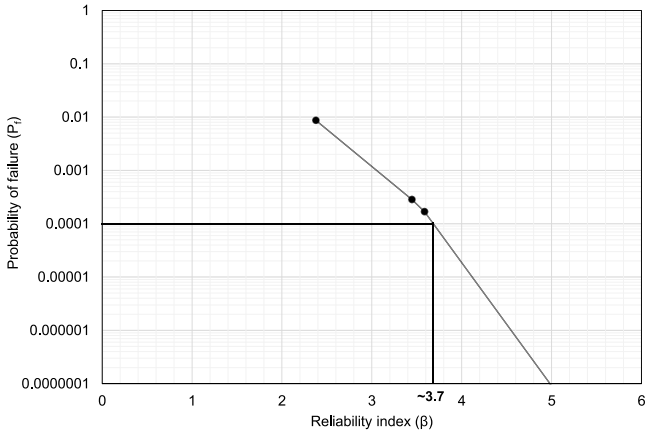

Fig. 14. Relationships between the reliability index and the probability of failure of this study. The trend line is generated by connecting the data points estimated for various scenarios.

Moreover, the evolution and extent of these faults (i.e., Vette, Tusse, Svart, Troll, etc.) are related (Stewart et al., 1995; Whipp et al., 2014), which indicated similar fault geometry and fault zone complexities in Vette fault as well. However, as case 1 is unlikely but a possible scenario, despite a low possibility, there are always chances of this event to happen, and if it occurs, the consequences will be significant. For instance, the probability of unsatisfactory performance for case 1 is 11 out of 1000, which belongs to the poor-to-unsatisfactory zone in the expected performance level (Table 8). To compare the poor and unsatisfactory level illustrated 23 and 70 failure events out of 1000 runs, respectively. On the other hand, the best-case scenario (case 4), where the Rødby Formation juxtaposes with the main reservoir rock (i.e., Sognefjord Formation), has very high fault seal probability (i.e., 0.7–1.0). Based on Færseth et al. (2007), the qualitative fault seal method shows a high uncalibrated shale gauge ratio (SGR). However, towards the south of the primary Vette fault, relay zones are formed, with cross-fault self-juxtaposition of the reservoir interval indicating low fault seal probability value (i.e., 0−0.3) (Mulrooney et al., 2018). There could be a possibility of pressure communication through this reservoir-reservoir juxtaposition. Still, the location is far from the proposed Alpha structure (south tipping point of the Vette fault) and might not be influential considering short post-injection time compare with the geological time frame (Fulljames et al., 1997). However, it is worth testing the scenario in any future numerical fluid flow model.

Table 8
The expected performances are based on the reliability index and the probability of failure values, adapted from U.S. Army Corps of Engineers (1997).

Expected Performance Level	Reliability index (β)	Probability of Unsatisfactory Performance[a]
High	5.0	0.0000003
Good	4.0	0.00003
Above average	3.0	0.001
Below average	2.5	0.006
Poor	2.0	0.023
Unsatisfactory	1.5	0.07
Hazardous	1.0	0.16

[a] Probability of unsatisfactory performance is the probability that the value of performance function will approach the limit state, or that an unsatisfactory event will occur.

The Draupne Formation shales could have been smeared in the early stage of the Vette fault; however, at present, the fault throw is significantly high near the Alpha structure, reducing the chances of smearing of this formation (Færseth, 2006). Fault rock strength equivalent to Sognefjord Formation is also unlikely as the fault interpreted in the 3D seismic (i.e., GN1101) is very sharp and seems to be a single surface. Moreover, there might be a possibility of sub-seismic resolution faults, which might change the likelihood of this case. However, the 3D seismic used for the structural interpretation (i.e., fault dip and definition of different scenarios) has good quality. Still, there are always interpretation-related uncertainties (i.e., human error, seismic quality, sub-seismic fault plane, etc.) present (Bond et al., 2015). The probabilistic approach such as this study incorporated those interpretation related uncertainties by using a probable data range. In contrast, the result of a deterministic method cannot include such a range and cannot cope with the uncertainties. Moreover, there might be the risk of biasness while assigning the probabilistic likelihood values for cases based on the geological understanding of that area. However, system reliability using the event tree method can significantly reduce that risk because the worst-case scenario dictates the final failure probability. For example, the Vette fault system PoF is within the 10^{-4} region, which is also the worst-case total probability of failure. If we change the likelihood number for other cases, the system failure number will be still within the 10^{-4} region. However, caution is needed to assign the worst-case scenario likelihood because if decreased tenfold, the system failure will be responding accordingly.

One of the positive findings is that the Vette fault failure probability decreases significantly with increasing the likelihood of the fault rock strength scenarios (Fig. 15). The higher the likelihood, the higher the possibility of the event to happen, hence increasing the possibility of sealing the Vette fault. Considering the geological interpretation with the failure probability, the Vette fault likely provides a structural trap for

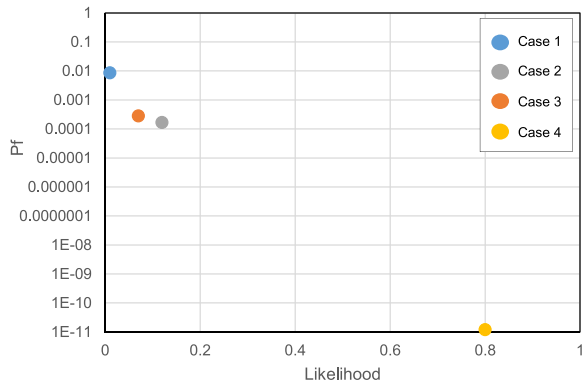

Fig. 15. Probability of failure (P_f) versus the likelihood of various fault rock strength scenarios of Vette fault in the initial condition.

the Alpha prospect; however, numerical modeling is required to evaluate the effect of the southward fault segment changes.

The reliability index (β) and the probability of failure (P_f) in any structure are a relative measurement of the current condition and provide a qualitative estimation of the expected performance (U.S. Army Corps of Engineers, 1997). Table 8 shows the β and P_f values with the corresponding performances to interpret structural safety. According to the chart (U.S. Army Corps of Engineers, 1997), the Vette fault system is in between the good to above-average performance range (i.e., β = ~3.7), which is also recommended by NORSOK standard Report (2010) for offshore installation. The unsatisfactory failure event for the Vette fault estimated is only 14 of 100000 results. Considering these published failure ranges, we can conclude that the Vette fault system's overall probability of failure is within the acceptable range and suggests that this fault may be a barrier in the potential Alpha structure.

The input parameters used to evaluate subsurface fault failure are often highly uncertain and cannot include all the uncertainties in the deterministic approach. However, the probabilistic method such as this study can integrate all the possible uncertain parameters with different ranges and can estimate the reliability; hence indicates the significance of the probabilistic approach in any structural integrity issues (i.e., fault seal analysis). Moreover, this study shows that integrating the likelihood of possible scenarios can result in different results than the case considering the only most likely scenario. In this way, the method considered all the possible worst-case scenario risks within the whole structural system reliability value; hence it was deemed more reliable. Also, the deterministic safety factor does not reflect the corresponding failure probability (Nadim, 2007). For example, Christian et al. (1994) illustrated a significantly different probability of failure for James Bay dikes for three height of dikes, where the factor of safety is similar. The probabilistic analysis can also explicitly show the trade-off between investment and reduction of potential losses, thus facilitating decision-making in the presence of uncertainties (Juang et al., 2019). In connection with the CO_2 storage sites, the structural system reliability value might thus simplify the future project decision.

This study shows that the methods used for system reliability analysis should be convenient and robust that can capture the risk of unlikely scenario. When the low failure probability of the case 4 was calculated, the crude Monte-Carlo simulation needs a significant number of iterations to get a result. It might be expensive and in some cases practically impossible. This study indicates that the FORM technique seems to be one of the appropriate method for this kind of subsurface static problems. When the limit state function is a smooth and monotonic function, which are typical for most of the static system, FORM can estimate the reliability index relatively accurately (Madsen et al., 2016). However, for the highly non-linear and high dimensional problems, which can often be for dynamic systems, FORM can result in a local minimum and consequently lead to an error (Fiessler et al., 1979). Thus, applying FORM for highly non-linear dynamic problems should be prudent. In further studies which calculate the stress conditions coupled with flow simulations using numerical methods (e.g., finite element method), other reliability approaches including optimized Monte Carlo simulations (e.g., importance sampling method) should be taken into account and the accuracy and efficiency should be tested.

The analytical solutions for the factor of random safety variables are usually represented as normal random variables with limited probability distribution options; hence numerical tools are necessary (Nomikos and Sofianos, 2011). However, assessing the possibility of evaluating the sensitivity of various input parameters in the analytical model is very convenient. This analysis will provide guidelines for future investigation. This study finds that the anisotropy of in-situ horizontal stress could be the most sensitive parameter for Smeaheia faults stability analysis; furthermore, the vertical stress and fault rock strength properties also have a significant impact. The in-situ stress field in Smeaheia needs further investigation for a better fault reliability understanding. In this study, we considered only 2D stress conditions by assuming the isotropic horizontal stress condition. The extended leak-off test database from the North Sea shows almost isotropic horizontal stress conditions for most North Sea hydrocarbon reservoirs (Andrews et al., 2016). However, 3D uncertainties along the fault plane could also be important when the probability of failure is near the marginal range. Besides, the pore pressure effect along the vertical section of fault might be critical to evaluate fault safety. Therefore, these parameters need further study before any future modeling work (i.e., analytical or numerical modeling approach).

6. Conclusion

The structural reliability of the Vette fault is the key to a successful Alpha structure CO_2 injection project. However, the parameters needed to evaluate the fault sealing integrity are highly uncertain. Therefore, we proposed this probabilistic reliability technique to estimate the structural failure likelihood of the Vette fault. The critical observations of this study are as follows:

- The cohesionless fault scenario has the highest failure probability, while the fault rock properties equivalent to the Rødby Formation case shows the lowest value. Moreover, the difference between the initial condition and the after-injection scenario is minimal.
- Both deterministic and probabilistic sensitivity analyses revealed that the in-situ stresses (vertical and horizontal) and fault rock strength properties (cohesion and friction angle) are the critical parameters influencing fault stability.
- Integrating the likelihood of possible scenarios using the event tree method can quantify the overall structural failure. The failure value estimated using this approach is the better representation of total failure compared to the case considering only the most likely scenario because the event tree method considered all the possible scenarios. However, caution needs to be taken for the low likelihood scenarios if the low likelihood scenario's failure probability is significantly higher than other likely scenarios.
- The Vette fault system reliability analysis' probabilistic value suggested that the fault seems to be structurally reliable. Hence, it may act as a potential barrier during the injection of CO_2 into the Alpha structure.

We can conclude that the probabilistic scenario-based event tree approach can be useful to quantify the subsurface structural reliability and proved to be a valuable tool in case considerable uncertainties are present.

CRediT authorship contribution statement

Md Jamilur Rahman: Conceptualization, Methodology, Formal

analysis, Investigation, Writing - original draft, Writing - review & editing, Visualization. **Jung Chan Choi:** Conceptualization, Methodology, Writing - review & editing, Supervision. **Manzar Fawad:** Writing - review & editing, Supervision. **Nazmul Haque Mondol:** Writing - review & editing, Supervision, Project administration, Funding acquisition.

Declaration of Competing Interest

The authors declare that they have no known competing financial interests or personal relationships that could have appeared to influence the work reported in this paper.

Acknowledgments

We are thankful for the funding provided by the Research Council of Norway for the OASIS (Overburden Analysis and Seal Integrity Study for CO_2 Sequestration in the North Sea) project (NFR-CLIMIT project #280472) and the FME NCCS Centre (NFR project #257579/E20). We are also grateful to Schlumberger™ for the Petrel-2018 academic software license, Python Software Foundation for Python, and Rick Allmendinger's Stuff for MohrPlotter.

References

Addis, M.A., 1997. The stress-depletion response of reservoirs. In: SPE Annual Technical Conference and Exhibition. Society of Petroleum Engineers. https://doi.org/10.2118/38720-MS.

Addis, M.A., Last, N.C., Yassir, N.A., 1994. The estimation of horizontal stresses at depth in faulted regions and their relationship to pore pressure variations. In: Rock Mechanics in Petroleum Engineering. Society of Petroleum Engineers. https://doi.org/10.2118/47289-MS.

Addis, M.A., Choi, X., Gunning, J., 1998. The influence of the reservoir stress-depletion response on the lifetime considerations of well completion design. In: SPE/ISRM Rock Mechanics in Petroleum Engineering. Society of Petroleum Engineers. https://doi.org/10.2118/28140-MS.

Andrews, J.S., Fintland, T.G., Helstrup, O.A., Horsrud, P., Raaen, A.M., 2016. Use of unique database of good quality stress data to investigate theories of fracture initiation, fracture propagation and the stress state in the subsurface. In: 50th US Rock Mechanics/Geomechanics Symposium. American Rock Mechanics Association.

Baklid, A., Korbol, R., Owren, G., 1996. Sleipner vest CO2 disposal, CO2 injection into a shallow underground aquifer. In: SPE Annual Technical Conference and Exhibition. Society of Petroleum Engineers. https://doi.org/10.2118/36600-MS.

Bohloli, B., Choi, J.C., Skurtveit, E., Grande, L., Park, J., Vannest, M., 2015. Criteria of Fault Geomechanical Stability During a Pressure Buildup. IEAGHG Rep. 4.

Bond, C.E., Johnson, G., Ellis, J.F., 2015. Structural model creation: the impact of data type and creative space on geological reasoning and interpretation. Geol. Soc. London Spec. Publ. 421, 83–97.

Bouvier, J.D., Kaars-Sijpesteijn, C.H., Kluesner, D.F., Onyejekwe, C.C., Van der Pal, R.C., 1989. Three-dimensional seismic interpretation and fault sealing investigations, Nun river Field, Nigeria. Am. Assoc. Pet. Geol. Bull. 73, 1397–1414. https://doi.org/10.1306/44B4AA5A-170A-11D7-8645000102C1865D.

Brændeland, G., Refsdal, A., Stølen, K., 2010. Modular analysis and modelling of risk scenarios with dependencies. J. Syst. Softw. 83, 1995–2013. https://doi.org/10.1016/j.jss.2010.05.069.

Campolongo, F., Kleijnen, J.P.C., Andres, T., 2000. Screening methods. Wiley Ser. Probab. Stat.Chiaramonte, L., White, J.A., Trainor-Guitton, W., 2015. Probabilistic geomechanical analysis of compartmentalization at the Snøhvit CO2 sequestration project. J. Geophys. Res. Solid Earth 120, 1195–1209. https://doi.org/10.1002/2014JB011376.

Chiaramonte, L., Johnson, S., White, J.A., 2011. Preliminary geomechanical analysis of CO2 injection at Snøhvit, Norway. In: 45th US Rock Mechanics/Geomechanics Symposium. American Rock Mechanics Association.

Childs, C., Walsh, J.J., Watterson, J., 1997. Complexity in fault zone structure and implications for fault seal prediction. Norwegian Petroleum Society Special Publications. Elsevier, pp. 61–72. https://doi.org/10.1016/S0928-8937(97)80007-0.

Christian, J.T., 2004. Geotechnical engineering reliability: how well do we know what we are doing? J. Geotech. Geoenviron. Eng. 130, 985–1003. https://doi.org/10.1061/(ASCE)1090-0241(2004)130:10(985).

Christian, J.T., Ladd, C.C., Baecher, G.B., 1994. Reliability applied to slope stability analysis. J. Geotech. Eng. 120, 2180–2207. https://doi.org/10.1061/(ASCE)0733-9410(1994)120:12(2180).

Ditlevsen, O., Madsen, H.O., 2007. Structural Reliability Methods. Internet e. ed.. John Wiley and Sons.

Doughty, P.T., 2003. Clay smear seals and fault sealing potential of an exhumed growth fault, Rio Grande rift, New Mexico. Am. Assoc. Pet. Geol. Bull. 87, 427–444. https://doi.org/10.1306/10010201130.

Dreyer, T., Whitaker, M., Dexter, J., Flesche, H., Larsen, E., 2005. From spit system to tide-dominated delta: integrated reservoir model of the Upper Jurassic Sognefjord Formation on the Troll West Field. Geological Society, London, Petroleum Geology Conference Series. Geological Society of London 423–448. https://doi.org/10.1144/0060423.

Duffy, O.B., Bell, R.E., Jackson, C.A.-L., Gawthorpe, R.L., Whipp, P.S., 2015. Fault growth and interactions in a multiphase rift fault network: horda Platform, Norwegian North Sea. J. Struct. Geol. 80, 99–119. https://doi.org/10.1016/j.jsg.2015.08.015.

Duncan, J.M., 2000. Factors of safety and reliability in geotechnical engineering. J. Geotech. Geoenviron. Eng. 126, 307–316. https://doi.org/10.1061/(ASCE)1090-0241(2000)126:4(307).

Easley, S.K., Pal, S., Tomaszewski, P.R., Petrella, A.J., Rullkoetter, P.J., Laz, P.J., 2007. Finite element-based probabilistic analysis tool for orthopaedic applications. Comput. Methods Programs Biomed. 85, 32–40. https://doi.org/10.1016/j.cmpb.2006.09.013.

Faber, M.H., 2009. Basics of Structural Reliability. Swiss Fed. Inst. Technol. ETH, Zürich, Switz.

Færseth, R.B., 2006. Shale smear along large faults: continuity of smear and the fault seal capacity. J. Geol. Soc. London. 163, 741–751. https://doi.org/10.1144/0016-76492005-162.

Færseth, R.B., Oppenboen, K.A., Saeboe, A., 1984. Trapping styles and associated hydrocarbon potential in norwegian North Sea. Am. Assoc. Pet. Geol. Bull. 68, 1201–1201.

Færseth, R.B., Johnsen, E., Sperrevik, S., 2007. Methodology for risking fault seal capacity: implications of fault zone architecture. Am. Assoc. Pet. Geol. Bull. 91, 1231–1246. https://doi.org/10.1306/03080706051.

Faleide, J.I., Bjørlykke, K., Gabrielsen, R.H., 2015. Geology of the Norwegian Continental Shelf. Petroleum Geosciences: From Sedimentary Environments to Rock Physics, pp. 603–637.

Faulkner, D.R., Jackson, C.A.L., Lunn, R.J., Schlische, R.W., Shipton, Z.K., Wibberley, C.A.J., Withjack, M.O., 2010. A review of recent developments concerning the structure, mechanics and fluid flow properties of fault zones. J. Struct. Geol. 32, 1557–1575.

Fiessler, B., Rackwitz, R., Neumann, H.-J., 1979. Quadratic limit states in structural reliability. J. Eng. Mech. Div. 105, 661–676.

Fisher, Q.J., Knipe, R.J., 2001. The permeability of faults within siliciclastic petroleum reservoirs of the North Sea and Norwegian Continental Shelf. Mar. Pet. Geol. 18, 1063–1081. https://doi.org/10.1016/S0264-8172(01)00042-3.

Foxford, K.A., Walsh, J.J., Watterson, J., Garden, I.R., Guscott, S.C., Burley, S.D., 1998. Structure and content of the Moab Fault Zone, Utah, USA, and its implications for fault seal prediction. Geol. Soc. London Spec. Publ. 147, 87–103. https://doi.org/10.1144/GSL.SP.1998.147.01.06.

Fulljames, J.R., Zijerveld, L.J.J., Franssen, R., 1997. Fault seal processes: systematic analysis of fault seals over geological and production time scales. Norwegian Petroleum Society Special Publications. Elsevier, pp. 51–59. https://doi.org/10.1016/S0928-8937(97)80006-9.

Gassnova, 2016. Feasibility Study for Full-scale CCS in Norway. https://ccsnorway.com/wp-content/uploads/sites/6/2019/09/feasibilitystudy_fullscale_ccs_norway_2016.pdf.

Geertsma, J., 1973. A Basic Theory of Subsidence Due to Reservoir Compaction; the Homogeneous Case.

Gibson, R.G., 1994. Fault-zone seals in siliciclastic strata of the Columbus Basin, offshore Trinidad. Am. Assoc. Pet. Geol. Bull. 78, 1372–1385. https://doi.org/10.1306/A25FECA7-171B-11D7-8645000102C1865D.

Grasso, J.-R., 1992. Mechanics of seismic instabilities induced by the recovery of hydrocarbons. Pure Appl. Geophys. 139, 507–534.

Gutierrez, M., Øino, L.E., Nygaard, R., 2000. Stress-dependent permeability of a demineralised fracture in shale. Mar. Pet. Geol. 17, 895–907. https://doi.org/10.1016/S0264-8172(00)00027-1.

Hackl, J., 2018. PyRe Documentation [WWW Document]. URL. http://github.com/hackl/pyre.

Hasofer, A.M., Lind, N.C., 1974. Exact and invariant second-moment code format. J. Eng. Mech. Div. 100, 111–121.

Hettema, M.H.H., Schutjens, P., Verboom, B.J.M., Gussinklo, H.J., 2000. Production-induced compaction of a sandstone reservoir: the strong influence of stress path. SPE Reserv. Eval. Eng. 3, 342–347. https://doi.org/10.2118/65410-PA.

Hillis, R.R., 2001. Coupled changes in pore pressure and stress in oil fields and sedimentary basins. Pet. Geosci. 7, 419–425. https://doi.org/10.1144/petgeo.7.4.419.

Holgate, N.E., Jackson, C.A.L., Hampson, G.J., Dreyer, T., 2015. Seismic stratigraphic analysis of the Middle Jurassic Krossfjord and Fensfjord formations, Troll oil and gas field, northern North Sea. Mar. Pet. Geol. 68, 352–380. https://doi.org/10.1016/j.marpetgeo.2015.08.036.

Horsrud, P., 2001. Estimating mechanical properties of shale from empirical correlations. SPE Drill. Complet. 16, 68–73. https://doi.org/10.2118/56017-PA.

Horsrud, P., Sønstebø, E.F., Bøe, R., 1998. Mechanical and petrophysical properties of North Sea shales. Int. J. Rock Mech. Min. Sci. 35, 1009–1020. https://doi.org/10.1016/S0148-9062(98)00162-4.

Hortle, A., Xu, J., Dance, T., 2013. Integrating hydrodynamic analysis of flow systems and induced-pressure decline at the Otway CO2 storage site to improve reservoir history matching. Mar. Pet. Geol. 45, 159–170.

IPCC, 2005. Carbon Dioxide Capture and Storage.

Jev, B.I., Kaars-Sijpesteijn, C.H., Peters, M.P.A.M., Watts, N.L., Wilkie, J.T., 1993. Akaso field, Nigeria: use of integrated 3-D seismic, fault slicing, clay smearing, and RFT

pressure data on fault trapping and dynamic leakage. Am. Assoc. Pet. Geol. Bull. 77, 1389–1404. https://doi.org/10.1306/BDFF8EA2-1718-11D7-8645000102C1865D.
Juang, C.H., Zhang, J., Shen, M., Hu, J., 2019. Probabilistic methods for unified treatment of geotechnical and geological uncertainties in a geotechnical analysis. Eng. Geol. 249, 148–161. https://doi.org/10.1016/j.enggeo.2018.12.010.
Karolytė, R., Johnson, G., Yielding, G., Gilfillan, S.M.V., 2020. Fault seal modelling–the influence of fluid properties on fault sealing capacity in hydrocarbon and CO2 systems. Pet. Geosci.
Kim, J., Berg, R.R., Watkins, J.S., Tieh, T.T., 2003. Trapping capacity of faults in the Eocene Yegua Formation, east sour lake field, southeast Texas. Am. Assoc. Pet. Geol. Bull. 87, 415–425. https://doi.org/10.1306/08010201129.
Lacasse, S., Nadim, F., 1998. Risk and Reliability in Geotechnical Engineering.
Lindsay, N.G., Murphy, F.C., Walsh, J.J., Watterson, J., Flint, S., Bryant, I., 1993. Outcrop studies of shale smears on fault surfaces. Geol. Model. Hydrocarb. Reserv. Outcrop Analog. 15, 113–123.
Madsen, H.O., Krenk, S., Lind, N.C., 2006. Methods of Structural Safety. Courier Corporation.
Martens, S., Kempka, T., Liebscher, A., Lüth, S., Möller, F., Myrttinen, A., Norden, B., Schmidt-Hattenberger, C., Zimmer, M., Kühn, M., 2012. Europe's longest-operating on-shore CO2 storage site at Ketzin, Germany: a progress report after three years of injection. Environ. Earth Sci. 67, 323–334. https://doi.org/10.1007/s12665-012-1672-5.
Mathieson, A., Midgley, J., Dodds, K., Wright, I., Ringrose, P., Saoul, N., 2010. CO 2 sequestration monitoring and verification technologies applied at Krechba, Algeria. Lead. Edge 29, 216–222.
Miocic, J., Johnson, G., Bond, C.E., 2019. Uncertainty in fault seal parameters: implications for CO2 column height retention and storage capacity in geological CO2 storage projects. Solid Earth.
Mulrooney, M.J., Osmond, J., Skurtveit, E., Wu, L., Braathen, A., 2018. Smeaheia, a potential northern North Sea co2 storage site: structural description and de-risking strategies, in: fifth CO2 Geological Storage Workshop. Eur. Assoc. Geoscient. Eng. 1–5. https://doi.org/10.3997/2214-4609.201802957.
Nadim, F., 2007. Tools and strategies for dealing with uncertainty in geotechnics. Probabilistic Methods in Geotechnical Engineering. Springer, pp. 71–95.
NESUS Theoretical Manual, 2011. Southwest Research Institute, San Antorio, Texas.
Nomikos, P.P., Sofianos, A.I., 2011. An analytical probability distribution for the factor of safety in underground rock mechanics. Int. J. Rock Mech. Min. Sci. 48, 597–605. https://doi.org/10.1016/j.ijrmms.2011.02.015.
NORSOK standard Report, 2010. Integrity of Offshore Structures.
NPD, 2020. NPD FactPages [WWW Document]. URL. https://factpages.npd.no/en/wellbore/PageView/Exploration/All/2918.
NPD CO2 Atlas, 2014. NPD CO2 Atlas Report.
Park, J.-W., Guglielmi, Y., Graupner, B., Rutqvist, J., Kim, T., Park, E.-S., Lee, C., 2020. Modeling of fluid injection-induced fault reactivation using coupled fluid flow and mechanical interface model. Int. J. Rock Mech. Min. Sci. 132, 104373 https://doi.org/10.1016/j.ijrmms.2020.104373.
Pereira, F.L.G., Roehl, D., Laquini, J.P., Oliveira, M.F.F., Costa, A.M., 2014. Fault reactivation case study for probabilistic assessment of carbon dioxide sequestration. Int. J. Rock Mech. Min. Sci. 71, 310–319. https://doi.org/10.1016/j.ijrmms.2014.08.003.
Plumb, R.A., 1994. Influence of composition and texture on the failure properties of clastic rocks. Rock Mechanics in Petroleum Engineering. Society of Petroleum Engineers.
Rock, L., O'Brien, S., Tessarolo, S., Duer, J., Bacci, V.O., Hirst, B., Randell, D., Helmy, M., Blackmore, J., Duong, C., 2017. The Quest CCS Project: 1st year review post start of injection. Energy Procedia 114, 5320–5328.
Rohmer, J., Seyedi, D.M., 2010. Coupled large scale hydromechanical modelling for caprock failure risk assessment of CO2 storage in deep saline aquifers. Oil Gas Sci. Technol. 65, 503–517. https://doi.org/10.2516/ogst/2009049 l'Institut Français du Pétrole.
Rutqvist, J., Birkholzer, J., Cappa, F., Tsang, C.-F., 2007. Estimating maximum sustainable injection pressure during geological sequestration of CO2 using coupled fluid flow and geomechanical fault-slip analysis. Energy Convers. Manage. 48, 1798–1807. https://doi.org/10.1016/j.enconman.2007.01.021.
Segall, P., 1989. Earthquakes triggered by fluid extraction. Geology 17, 942–946. https://doi.org/10.1130/0091-7613(1989)017<0942:ETBFE>2.3.CO;2.
Skerlec, G.M., 1996. Risking Fault Seal in the Gulf Coast (Abs.): AAPG Annual Convention Program and Abstracts, v. 5, p. A131.
Skurtveit, E., Grande, L., Ogebule, O.Y., Gabrielsen, R.H., Faleide, J.I., Mondol, N.H., Maurer, R., Horsrud, P., 2015. Mechanical testing and sealing capacity of the Upper Jurassic Draupne Formation, North Sea. 49th US Rock Mech. Symp. Am. Rock Mech. Assoc.
Skurtveit, E., Choi, J.C., Osmond, J., Mulrooney, M., Braathen, A., 2018. 3D fault integrity screening for smeaheia CO2 injection site. 14th Greenhouse Gas Control Technologies Conference Melbourne 21–26.
Stewart, D.J., Schwander, M., Bolle, L., 1995. Jurassic depositional systems of the Horda Platform, Norwegian North Sea: practical consequences of applying sequence stratigraphic models. Nor. Pet. Soc. Spec. Publ. 291–323. https://doi.org/10.1016/S0928-8937(06)80073-1.
Thoft-Christensen, P., Baker, M.J., 1982. Reliability of structural systems. Structural Reliability Theory and Its Applications. Springer, Berlin, Heidelberg, pp. 113–127.
U.S. Army Corps of Engineers, 1997. Engineering and Design Introduction to Probability and Reliability Methods for Use in Geotechnical Engineering. Washington, D.C..
Verdon, J.P., Kendall, J.M., Stork, A.L., Chadwick, R.A., White, D.J., Bissell, R.C., 2013. Comparison of geomechanical deformation induced by megatonne-scale CO2 storage at Sleipner,Weyburn, and in Salah. Proc. Natl. Acad. Sci. 110, E2762–E2771. https://doi.org/10.1073/pnas.1302156110.
Vidal-Gilbert, S., Tenthorey, E., Dewhurst, D., Ennis-King, J., Van Ruth, P., Hillis, R., 2010. Geomechanical analysis of the Naylor Field, Otway Basin, Australia: implications for CO2 injection and storage. Int. J. Greenh. Gas Control 4, 827–839. https://doi.org/10.1016/j.ijggc.2010.06.001.
Walsh, J.J., Watterson, J., Heath, A.E., Childs, C., 1998. Representation and scaling of faults in fluid flow models. Pet. Geosci. 4, 241–251. https://doi.org/10.1144/petgeo.4.3.241.
Whipp, P.S., Jackson, C.L., Gawthorpe, R.L., Dreyer, T., Quinn, D., 2014. Normal fault array evolution above a reactivated rift fabric; a subsurface example from the northern Horda Platform, Norwegian North Sea. Basin Res. 26, 523–549. https://doi.org/10.1111/bre.12050.
Wiprut, D., Zoback, M.D., 2000. Fault reactivation and fluid flow along a previously dormant normal fault in the northern North Sea. Geology 28, 595–598. https://doi.org/10.1130/0091-7613(2000)28<595:FRAFFA>2.0.CO;2.
Yielding, G., 2002. Shale gouge ratio—calibration by geohistory. Nor. Pet. Soc. Spec. Publ. 11, 1–15. https://doi.org/10.1016/S0928-8937(02)80003-0.
Yielding, G., Freeman, B., Needham, D.T., 1997. Quantitative fault seal prediction. Am. Assoc. Pet. Geol. Bull. 81, 897–917. https://doi.org/10.1306/522B498D-1727-11D7-8645000102C1865D.
Zieglar, D.L., 1992. Hydrocarbon columns, buoyancy pressures, and seal efficiency: comparisons of oil and gas accumulations in California and the Rocky Mountain area. Am. Assoc. Pet. Geol. Bull. 76, 501–508. https://doi.org/10.1306/BDFF884E-1718-11D7-8645000102C1865D.
Zoback, M.D., 2010. Reservoir Geomechanics. Cambridge University Press. Case.